# Multiphysics Coupling in Lithium-Ion Batteries with Reconstructed Porous Microstructures

Sangwook Kim, Junghyun Wee, Kara Peters, and Hsiao-Ying Shadow Huang*

Mechanical and Aerospace Engineering Department, North Carolina State University, Raleigh, North Carolina 27695, United States

ABSTRACT: For an energy storage application such as electrical vehicles (EVs), lithium-ion batteries must overcome limited lifetime and performance degradation under specific conditions. Particularly, lithium-ion batteries show significant capacity loss at higher discharging rates (C-rates). In this work, we develop computational models incorporating coupled electrochemical–mechanical–thermal factors in order to reveal the relationship between the experimentally observed capacity loss and predicted mechanical stresses during electrochemical (dis)charging. Specifically, a multiphysics finite element model consisting of electrochemistry, heat generation, mass transport, and solid mechanics is developed to investigate thermal- and diffusion-induced stresses with the reconstructed porous microstructures of commercial $LiFePO_4$ batteries. It has been suggested that porous microstructures in electrodes could mitigate the electrolyte reactivity for an improved battery life and safety. Therefore, the reconstructed porous microstructures from focused ion beam–scanning electron microscopy (FIB-SEM) images are adopted. The integrated experimental measurements and computational simulations show that: (1) Lithium-ion cells electrochemically tested at 3.6C have 30% capacity loss versus cells tested at 1.2C; a corresponding stress increase of 150% is observed from the multiphysic simulations. (2) The thermal models verified by *in operando* temperature measurement via the fiber Bragg grating (FBG) sensor demonstrate that increasing temperature results in larger thermal stresses during (dis)charging. However, increases in thermal stress due to higher temperature played a lesser role at higher C-rates. (3) Lithium-ion concentration distribution is location dependent; that is, at any time and at any given C-rate, the outer layer of the particle exhibits a higher concentration than that inside the particle. (4) Higher diffusion-induced stresses are observed at the connecting areas between particles, suggesting that the higher stresses may result from higher concentration variations in the connecting area. This study presents results that include evolutions of lithium-ion concentration and mechanical stresses and could help to provide insight into the decreasing electrochemical performance of lithium-ion batteries at higher C-rates.
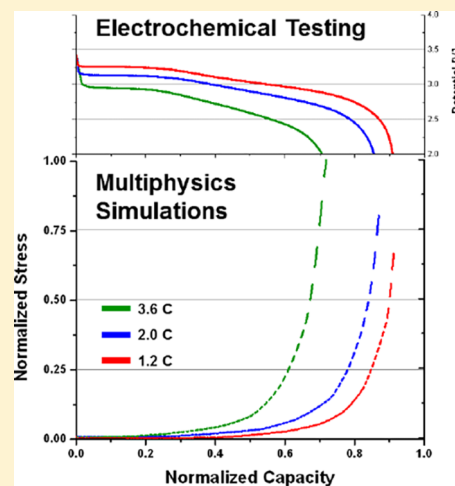
1. INTRODUCTION

Because of the increasing market share of electric vehicles (EVs), the importance of electrochemical energy storage systems is increasing continuously. High energy density makes lithium-ion batteries a practical solution to be utilized as an energy storage system in EVs. However, difficulty retaining the lithium-ion battery capacity has been observed at high C-rates and long cycle lives.[1−3] It has been suggested that the performance and the lifetime of lithium-ion batteries are directly correlated with the effectiveness and stability of the electrode−electrolyte interfaces.[3−6] It is well-known that the structural changes in electrode materials, including volume expansions ranging from ∼2−7% in cathodes and ∼200−300% in anodes,[7−13] are often reported to be a key factor in the deterioration of lithium-ion battery performance. Indeed, irreversible changes are introduced that render the battery unfit for applications requiring high energy storage. As a result, transport properties such as the rate of ion diffusion and migration through the electrolyte, electrodes, or the electrode−electrolyte interfaces could be altered. Moreover, volume expansion and exothermic reactions generate additional mechanical and thermal energy during (dis)charge, which could result in the inhomogeneous distribution of strain near electrode surfaces. Results to date have yet to delineate how these relationships affect the physical phenomena at the electrode−electrolyte interfaces; thus, the scientific underpinnings required for the design of next generation electrochemical energy storage remain elusive.

Many studies focus on the effects of the solid−electrolyte interface (SEI) films, which cause the deterioration in the surface structures of the electrode and generally result in aging in anode materials.[14−20] Specifically, during the first several (dis)charging cycles in lithium-ion batteries, reductive electrolyte decomposition accompanied by irreversible consumption of lithium ions takes place at the SEI when the anode is in the charged state. SEI layers are also found in cathodes. When voltages are above the oxidation potential of the electrolyte, understanding and controlling SEI formation at the cathode

A

become very important. Across the range of SEI studies, chemical engineers, material scientists, and electrochemists have reported their findings on (electro)chemical reactions, material stability, and the associated kinetics. Yet, a fundamental understanding of the relationships between charge and mass transport properties, structural changes, and thermal and mechanical stresses at the electrode–electrolyte interface is still lacking. For example, Aurbach et al.[6,21] have studied the effects of acidic and nonacidic electrolytes on carbon-coated $LiFePO_4$ cathodes during storage period by measuring Fe ion dissolution (the chemical reaction of rusting). Fe ion dissolution represents the loss of the active mass from the electrode, indicating that the cathode is deteriorated. As expected, higher temperature leads to more dissolution of Fe ions. The study showed that the electrolyte becomes more acidic at higher temperature, and the dissolution of Fe ions becomes pronounced, causing unstable behavior in the electrode.[6,21] These observations suggest that temperature-related chemical reactions in cathodes appear to be important determinants of the charge transport property and structural responses at the cathode–electrolyte interface.

Studies have shown that lithium-ion battery performance is highly dependent on temperature. Once the temperature of a lithium-ion cell at full charge exceeds a predetermined set point, the possibility of a thermal runaway becomes a serious concern.[22,23] Liu et al.[24] developed framework models incorporating mechanical effects, short-circuit, thermal runaway, and thermal submodels in batteries and demonstrated temperature rising behavior during abusive conditions. Xu's research group continues moving forward on better understanding interactions between these factors.[25,26] To measure temperature variation due to heat generation in the lithium-ion battery, several methods such as thermocouples,[27–30] infrared images,[30,31] and gold-resistance temperature detectors[32] have been used. However, the aforementioned methods are not able to measure the temperature inside of the battery (i.e., the cathode layer surrounded by electrolyte). Thus, fiber Bragg grating (FBG) is an attractive sensor for the temperature measurement due to its immunity against electromagnetic interference and the surrounding electrolyte. Specifically, FBG is a narrow band wavelength filter inscribed in an optical fiber. It can measure mechanical strain and temperature based on the reflected wavelength shifts due to applied strain and temperature.[33] Meyer et al.[34] verified the accuracy of FBG sensors for temperature measurement by comparing to a thermistor measurement. Moreover, Novais et al.[35] successfully measured the external and internal temperatures in lithium-ion batteries by using FBG sensors.

It has been suggested that heat generation could initiate electrolyte ignition, resulting in thermal runaway and explosion.[27] This is strongly related to electrochemical and mechanical degradation of battery materials. Computational thermal analysis in lithium-ion batteries has been studied by many groups to relate the degradation in lithium-ion batteries with excessive temperature rise under high C-rate. Zhang et al.[36] investigated heat generation and intercalated-induced stresses in $LiMn_2O_4$ single particles and concluded that those two factors are coupled to each other and should be considered simultaneously. The computational model developed by Wu et al.[37] also demonstrates that intercalation and thermal expansion occur in both electrode and electrolyte concurrently and are not a simple summation. The same research group, as well as Xiao et al.[38] and Wu et al.,[39] reported that the thermal stress is

comparable to or even higher than the diffusion-induced stress in the separator. Furthermore, Yan et al.[40] investigated heat generation in a reconstructed $LiCoO_2$ instead of simple core–shell particles. To further understand diffusion-induced stresses in lithium-ion batteries, current state-of-the-art on the computational modeling is moving toward reconstructed geometries of electrodes.

Early stage researches had used simple geometries such as spheres, spheroids, cylinders, and discs in Newman's pseudo-2D model to analyze diffusion-induced stresses in cathode materials[36,38,41,42] while recognizing that stress development has a major impact on the performance of lithium-ion batteries.[43] However, there were still limitations when simple geometries were used because they failed to predict the phenomena relating to the inhomogeneous natures of the electrode microstructures.[44] To overcome the limitations of using a simple geometry, realistic microstructures reconstructed based on X-ray nanoscale computer tomography (CT)[40,44,45] and focused ion beam–scanning electron microscopy (FIB-SEM)[46–52] have gained significant attention. Specifically, $LiCoO_2$ current density, overpotential intercalation rate,[40] electrostatic potential,[46] and microstructural parameters[48] have been investigated with microstructure geometry. Ender et al.[48] demonstrate significant parameters including particle size, active surface area, and tortuosity of $LiFePO_4$ with FIB/SEM. Furthermore, lithium concentration distribution in $LiFePO_4$ electrodes was investigated by Kashkooli et al.[44] An increasing number of researchers have used microstructure geometry for stress analysis. Song et al.[52] tried to explain particle fragmentation in $Li(Li_{0.2}Mn_{0.54}Ni_{0.13}Co_{0.13})O_2$ (LLMNC) using the predicted stress based on a simple mathematical model with microstructure geometry. Moreover, Wu et al.[45] investigated mechanics in nickel–manganese–cobalt (NMC), showing that concave and convex regions of stress concentration are crucial. However, the effects of electrolyte in mechanical and thermal stress were not considered in these studies.

In this paper, we developed a multiphysic computational model based on the reconstructed microstructure of $LiFePO_4$ obtained by FIB-SEM, and we studied the relationships between temperature, volume change, thermal stresses, and diffusion-induced stresses to address their coupling effects on the electrochemical performance in lithium-ion batteries. Therefore, the goal of this study is to integrate experimental and computational approaches which consider charge/mass transport properties, structural changes, and thermal and mechanical stresses at the electrode–electrolyte interfaces to understand the relationships between the capacity loss over a range of charging rates (i.e., C-rate), temperature, and lithium-ion concentration.

2. METHODS

2.1. Electrochemical Testing. Rate capability electrochemical testing on 14 430 lithium-ion cells (400 mAh; Battery Space, Richmond, CA) was performed via a 273A potentiostat/galvanostat (EG&G Princeton Applied Research, Oak Ridge, TN) at four different discharging rates (0.6C, 1.2C, 2.0C, and 3.6C). 0.6C charging rate was used between each discharging, whereas the potential was set between 2.0 and 4.0 V. A data acquisition board 6052E and LabVIEW Robotics 2013 (National Instruments, Austin, TX) were used to communicate between the potentiostat and the computer to obtain the capacity fade of the battery cells. During the electrochemical
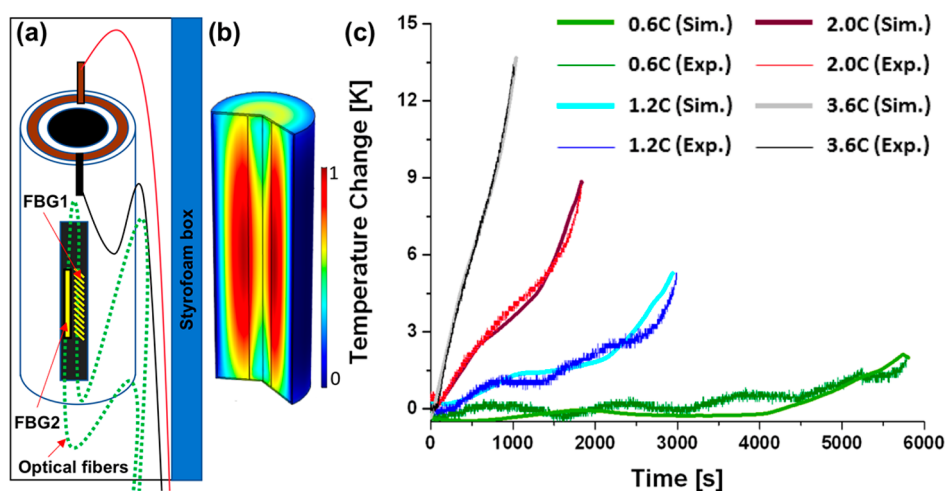
Figure 1. (a) Representative diagram of *in operando* temperature measurement by FBG sensors at the electrode−electrolyte interface during electrochemical testing. The battery and FBG sensors were located inside a styrofoam box to minimize convective heat transfer. (b) To better understand temperature effects on electrochemical and mechanical battery material degradation, our pilot study has demonstrated that an axisymmetric heat transfer mechanism could be used for computational simulations. (c) Greater temperature change due to higher Joule heating at higher C-rate was observed. It was observed that at the beginning and the end of the discharging process the temperature gradient was higher than that of the plateau region during discharging for all measured and simulation cells.
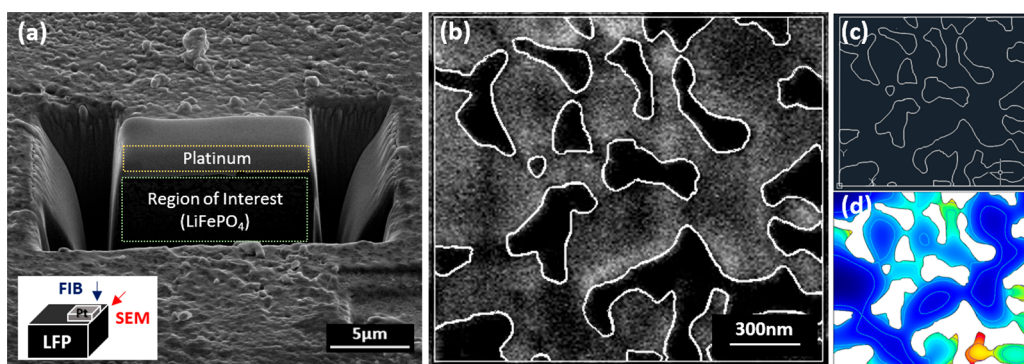

Figure 2. (a) SEM image of LiFePO$_4$ sample during FIB micromilling under high vacuum (e.g., 10^{-6} Pa). Platinum was first deposited on the surface of LiFePO$_4$ to prevent the curtaining effect. (b) Original SEM image of 1.5×1.5 μm^2 with higher magnification (>15000×) and image after image processing were overlapping (white line indicated particle boundary after image processing). (c) An image was converted into a dxf file format for computational simulation. (d) A representative concentration distribution of the reconstructed porous microstructures of LiFePO$_4$ (50% state of charge at 1.2C).

testing, the total (dis)charging time was also recorded. To ensure the temperature was recovered to the ambient temperature (20 °C) during discharging and charging, an adequate resting time over 30 min was included after each electrochemical (dis)charging cycle.

2.2. Temperature Measurement by Fiber Bragg Grating (FBG) Sensor. A fiber Bragg grating (FBG) sensor was used for the *in operando* measurements of strain and temperature variations at the electrode−electrolyte interface during the electrochemical testing. The FBG sensor has 1 cm grating length with 15 μm thick polyimide coating (Micrometer Optics. Inc., Atlanta, GA). The sensor was connected to an optical interrogator (Micrometer Optics. Inc., Atlanta, GA) to track the peak wavelength shift as a function of the temperature with the precision of ±1 pm. The sampling rate was 1 sample/s, which was sufficient for the measurement of quasi-static temperature change. Layers encapsulating the cathode and anode in a commercial LiFePO$_4$ battery, such as heat shrink wrap and outer aluminum can, were removed to measure the temperature inside the cell. The FBG sensor for the

temperature measurement was mechanically decoupled from the cathode surface but was placed on the surface of the cathode in order to ensure accurate and concurrent temperature measurement along with the mechanical strains.[34] Moreover, the battery and FBG sensor were sealed inside a styrofoam box to minimize convective heat transfer (Figure 1a,b). The wavelength shift of the FBG with respect to the temperature change is expressed with the following equation:[33]

$$\Delta\lambda = \lambda_B(\alpha_s + \varsigma)\Delta T \qquad (1)$$

where λ_B is the Bragg wavelength, ΔT is the temperature change, α_s is the thermal expansion coefficient of silica, and ς is the thermo-optic coefficient of silica. For the fused-silica optical fiber, the sum of the two coefficients is $\alpha_s + \varsigma = 6.67 \times 10^{-6}$ °C^{-1}.[33] Note that all temperature changes were measured with respect to the ambient temperature (20 °C).

2.3. Reconstructed Electrode Microstructure by FIB/SEM. To generate reconstructed electrode microstructures, separate sets of uncycled commercial lithium-ion batteries (LiFePO$_4$, 14 430 cells) were disassembled in an argon-filled

Table 1. List of Model Parameters[44,60−64]

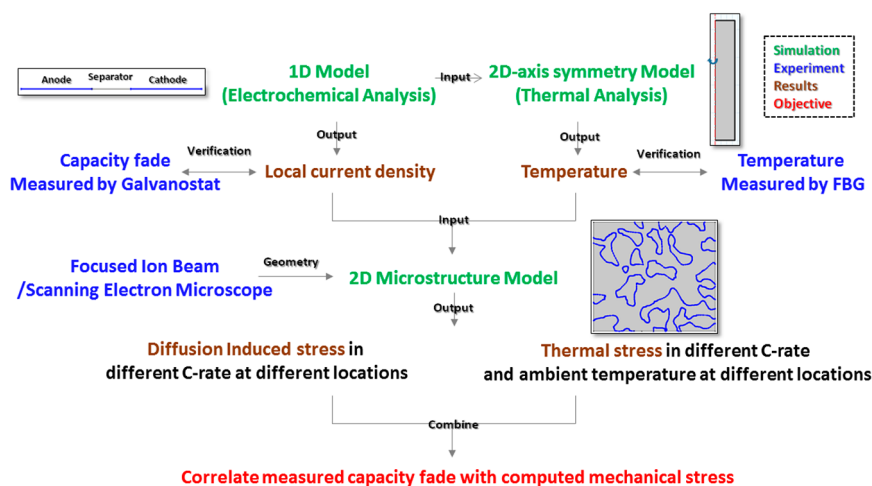|	anode	separator	cathode	unit
thickness (δ)	55	33	55	μm
electrical conductivity (σ_s)	1×10^4		3.5×10^{-5}	s/cm
ionic conductivity (σ_l)		10.7		s/cm
maximum solid phase concentration ($C_{s,max}$)	3.108×10^4		2.28×10^4	mol/m^3
charge transfer coefficient (α_a, α_c)	0.5		0.5	
transport number (t_+)		0.343		
diffusion coefficient (D)	3.2×10^{-10}	2.6×10^{-6}	1.3×10^{-9}	cm^2/s
reaction rate constants (k_a, k_c)	1.764×10^{-11}		2.5×10^{-13}	m$^{2.5}$ mol$^{-0.5}$/s

Figure 3. Outline of this research. First of all, electrochemistry analysis has been done in a 1D model, composed of negative electrode, electrolyte, and positive electrode. In the 1D analysis, local current density and potential changes according to time in the positive electrode were computed. The computed results were compared with data from experimental measurements to verify the 1D electrochemical model. This procedure has continuously repeated until the model was verified. Moreover, heat generation was computed in the 1D model, and it transferred to the 2D-axis symmetry model for thermal analysis. Based on the computed heat generation, the temperature distribution in the cylindrical cell was calculated. Since the temperature on the surface of cylindrical cell was measured by FBG sensor, simulated temperature on the outer layer was compared with experimental results to verify the thermal analysis. Verified local current density and temperature were used in 2D microstructure model. Local current density was major boundary conditions for concentration distribution in electrode particles. After calculating the concentration distribution in the electrode, diffusion-induced stresses were computed. Furthermore, thermal stress was computed based on the temperature boundary conditions. Compared to the electrode particle sizes, the thermal conductivity was relatively high; thus, a nearly constant temperature distribution was observed.

glovebox (Precise Controlled Atmosphere Glove Box, Labconco, Kansas City, MO). *N*-Methyl-2-pyrrolidone (NMP) was used to clean the surface of LiFePO$_4$ samples for the focused ion beam−scanning electron microscope (FIB-SEM). In this study, FEI Quanta 3D FEG (FIB-SEM) at the NC State Analytical Instrument Facility (AIF) was used for micromilling with FIB and taking SEM images at different angles (i.e., 54° in this facility) with high resolution (Figure 2a). Platinum was first deposited on the surface of LiFePO$_4$ to prevent the curtaining effect, which could increase surface roughness in the direction of the milling depth and result in stripes on the cutting surface, and eventually the roughness of the cut could influence the measurements and the segmentation process. To focus on the region of interest (ROI), each side of the ROI was milled by FIB. For more detailed particle configuration, a sector of 1.5×1.5 μm^2 with higher magnification (>15000×) was used (Figure 2b). The pixel size of the scanning electron microscopy (SEM) images was 8.28 nm. The image processing, including smooth processing, edge finding processing, and threshold determination, was conducted using ImageJ image analysis software (National Institutes of Health, Bethesda, MD). Because of the high magnification, it was relatively difficult to distinguish the

boundary between the cathode and electrolyte; therefore, smooth processing was necessary to obtain better binary images before using the "find-edge plugin" in ImageJ. After identifying the boundary with the aforementioned plugin, the image of LiFePO$_4$ reconstructed microstructure was converted to a binary image using the "threshold plugin" in ImageJ. To import the 2D configuration into the finite element software, a specific file format—the dxf file (commonly used in AutoCAD)—was required. In this work, ReaConverter 7 (Realsoft Inc., Monmouth Junction, NJ) was then used to convert the LiFePO$_4$ microstructure from the binary image to a dxf file, as shown in Figure 2c.

2.4. Multiphysic Computational Model. The reconstructed LiFePO$_4$ microstructure was used to develop multiphysic finite element models of a half-cell system (i.e., with electrolyte and cathode) via COMSOL Multiphysics (COMSOL, Inc., Burlington, MA), in which electrochemical reactions, charge/mass transport, heat conduction, and solid mechanics were included. The parameters used in multiphysic computational model are tabulated in Table 1. The outline of our multiscale model and experiment in this research is presented in Figure 3, where we detailed our integrated electrochemistry, thermal, and mechanical analysis by incorporating galvanostat
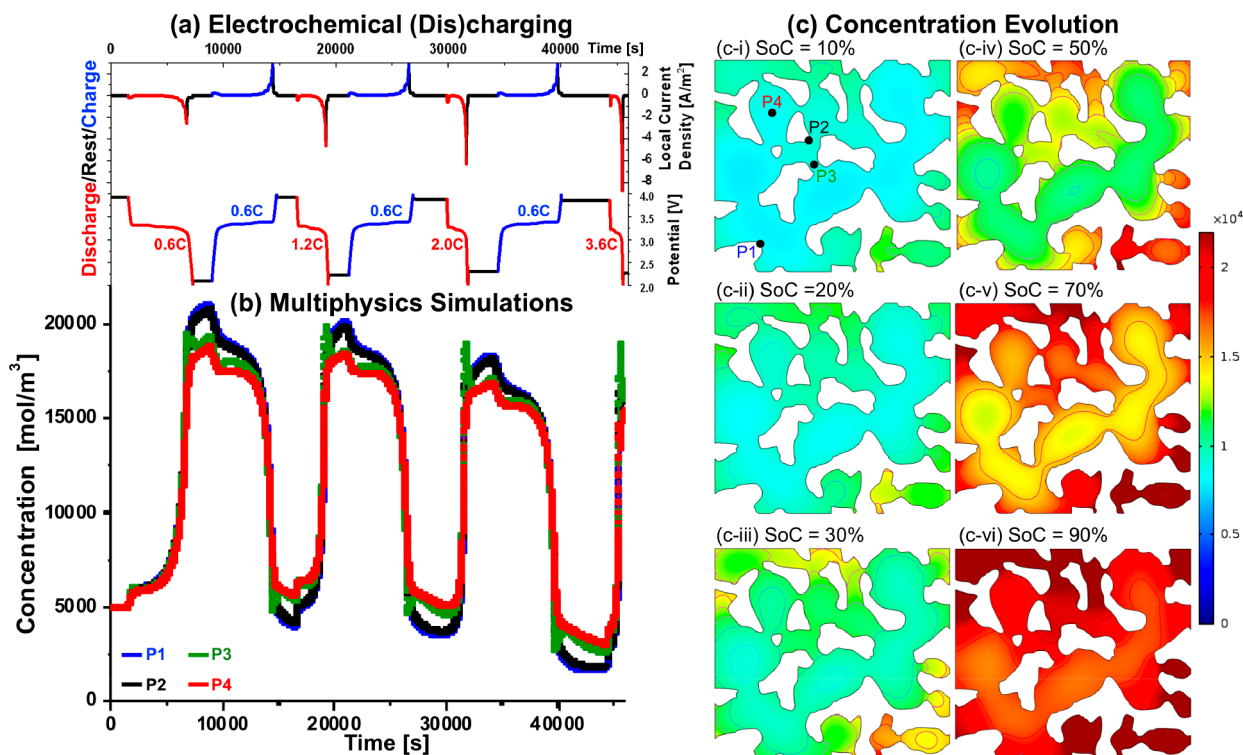
Figure 4. (a) Local current density and potentials vs time for multiphysic computational simulations. Four different discharging rates (0.6C, 1.2C, 2.0C, and 3.6C) and 0.6C charging rate were used between each discharge cycle, whereas the potential was set between 2.0 and 4.0 V. (b) Concentration variations at four different locations (P1, P2, P3, and P4 in (c)) were compared. It was observed that higher concentration gradient existed at the connecting areas of the particles (P3 vs P4). (c) Concentration evolutions at different SoCs. It was observed that smaller particles exhibited higher concentrations, compared to larger particles, which could be due to much more dramatic concentration changes existing in smaller particles.

for current density measurements, FIB/SEM to generate porous microstructure, and FBG sensors to conduct temperature measurements.

2.4.1. Electrochemistry. We developed the 1D model, composed of anode, separator, and cathode, to investigate the physical behavior of the electrolyte−electrode interface in the Batteries and Fuel Cells Module of COMSOL Multiphysics.[53] Specifically, the conservation of the current density in the electrolyte was incorporated by the following equation:

$$\nabla \cdot i_l = 0 \tag{2}$$

where i_l is the current density in the electrolyte, which satisfies the following kinetic equation:

$$i_l = -\sigma_l \nabla \phi_l + \frac{2\sigma_l RT}{F}\left(1 + \frac{\partial \ln f}{\partial \ln c_l}\right)(1 - t_+)\nabla \ln c_l \tag{3}$$

where σ_l denotes the ionic conductivity in electrolyte, ϕ_l is the electric potential in the electrolyte, R is the gas constant, T is temperature, F is the Faraday constant (96 485 C/mol), $\frac{\partial \ln f}{\partial \ln c_l}$ is activity dependence (assumed to be 1), and t_+ is the transport number. The molar flux vector of lithium ions (J_l) was calculated based on both diffusion and migration in the electrolyte, expressed by the following equation:

$$J_l = -D_l \nabla c_l + \frac{i_l t_+}{F} \tag{4}$$

where D_l is the diffusion coefficient in the electrolyte.

In the electrode, the conservation of current density in the electrode is governed by Ohm's law, as shown below:

$$\nabla \cdot i_s = 0, \quad i_s = -\sigma_s \nabla \phi_s \tag{5}$$

where i_s is the current density, σ_s is the electrical conductivity of electrode, and ϕ_s is the electrical potential in the electrode. The molar flux vector of lithium ions in electrode (J_s) is expressed by Fick's first law:

$$J_s = -D_s \nabla C_s \tag{6}$$

where D_s is the diffusion coefficient in the electrode and C_s is the lithium-ion concentration in the cathode.

To model electrode−electrolyte interfaces, the local current density at the interface between the electrolyte and the electrode (i_{loc}) is defined by the Butler−Volmer equation:

$$i_{loc} = i_0\left(\exp\left(\frac{\alpha_a F \eta}{RT}\right) - \exp\left(\frac{-\alpha_c F \eta}{RT}\right)\right) \tag{7}$$

where α_a and α_c are anodic and cathodic charge transfer coefficients, η is the overpotential, and i_0 is the exchange current density, as detailed below:

$$i_0 = F(k_c)^{\alpha_a}(k_a)^{\alpha_c}(C_{s,max} - C_s)^{\alpha_a}(C_s)^{\alpha_c}\left(\frac{C_l}{C_{l,ref}}\right)^{\alpha_a} \tag{8}$$

where k_a and k_c are anodic and cathodic reaction rate constants, respectively, and $c_{l,ref}$ is the electrolyte reference concentration. The computed local current density at the interface (i_{loc}) (eq 7) during electrochemical cycling was then used as a boundary condition for simulations of ionic mass/charge transport. A representative concentration distribution of the reconstructed porous microstructures of LiFePO$_4$ is shown in Figure 2d.

Moreover, the corresponding overpotential is defined as follows:

$$\eta = \phi_s - \phi_l - E_{eq} \tag{9}$$

where ϕ_s is the solid phase potential, ϕ_l is the electrolyte phase potential, and E_{eq} is the equilibrium potential. To reduce computational time, the effect of the solid−electrolyte interface was not considered in this model. In the computational simulations, electrochemical (dis)charging sequences followed experimental electrochemical testing, as described in section 2.1. Briefly, the electrode was discharged at 0.6C (2000−8000 s), 1.2C (17 000−20 000 s), 2.0C (30 400−32 200 s), and 3.6C (45 000−46 000 s); 0.6C charging rate was used between each discharge (9450−15 200 s, 21 600−27 300 s, and 34 900−40 500 s). The cycle also included an open-circuit period (applied current is 0 A/m^2) between each charging and discharging process (0−2000 s, 9000−9450 s, 15 200−17 000 s, 20 000−21 600 s, 27 300−30 400 s, and 32 200−34 900 s), as shown in Figure 4a.

2.4.2. Transport of Lithium Ions in Cathode. 2D mass/charge transport of lithium ions in the cathode material was incorporated into the multiphysic simulations. Since composition-independent transport properties such as D_l and D_s were used in this study, transport of diluted species was considered to describe the lithium-ion diffusion and migration in the half-cell system. Moreover, the computed local current density at the interface (i_{loc}) from eq 7 in 1D electrochemistry model was used as a boundary condition for ionic mass/charge transport simulation. The initial concentration of lithium ions in the cathode material was assumed to be homogeneous with a value of 5000 mol/m^3 in this study. Based on Fick's second law of diffusion (eq 10), the concentration distribution in cathode material was then computed. The calculated concentration in the active particles was then transferred to the solid mechanics model for diffusion-induced stress prediction.

$$\frac{\partial C}{\partial t} = D_s(\nabla^2 C) \tag{10}$$

2.4.3. Axisymmetric Heat Transfer. Studies have shown that temperatures in excess of 45 °C will rapidly degrade the battery lifetime, and higher temperatures can also introduce safety concerns as materials contained within the battery can begin to chemically and mechanically degrade.[54] To better understand temperature effects on electrochemical and mechanical battery material degradation, our pilot study which incorporated the physical dimensions of the LiFePO$_4$ 14 430 cells has demonstrated that an axisymmetric heat transfer mechanism could be used for computational simulations (Figure 1b). The 2D axisymmetric heat transfer model is represented as follows:

$$\rho C_p\left(\frac{\partial T}{\partial t}\right) + \nabla\cdot(k\nabla T) - h(T_{ext} - T) = Q \tag{11}$$

where ρ is the density, C_p is the specific heat capacity, k is the thermal conductivity, T is absolute temperature, T_{ext} is the external absolute temperature, h is the heat transfer coefficient, and Q is the heat source. Based on eq 11, the radial temperature distribution was calculated by assuming that specific heat capacity, thermal conductivity, and the heat transfer coefficient were constant during electrochemical cycling. The material properties used in eq 11 are listed in Table 2.

Heat generation in lithium-ion batteries is mainly caused by Joule heat due to charge transport, reversible entropy heat, heat

Table 2. Thermal Properties of Cathode and Electrolyte[31,38,65]

component	parameter	value	unit
cathode (LiFePO$_4$)	thermal conductivity (k_c)	1.48	W/(m °C)
	specific heat capacity ($C_{p,c}$)	1260.2	J/(kg °C)
	thermal expansion (α_c)	4.6×10^{-5}	1/K
electrolyte (LiPF$_6$ in EC-DMC)	thermal conductivity (k_l)	0.099	W/m °C
	specific heat capacity ($C_{p,l}$)	1800	J/(kg °C)
	thermal expansion (α_l)	1×10^{-3}	1/K

from chemical side reactions, and heat of mixing due to the generation and relaxation of lithium-ion concentration gradients.[55] In this study, only Joule heating was considered and the contribution from other heat sources were neglected since they were relatively less critical in lithium-ion batteries.[39] Joule heat (Q_{JH}) generated by the charge transport in the electrodes and the electrolyte is expressed by the following equation:

$$Q_{JH} = -(i_s\cdot\nabla\phi_s + i_l\cdot\nabla\phi_l) \tag{12}$$

2.4.4. Solid Mechanics. Thermal- and diffusion-induced stresses and strains in the electrode were obtained in the solid mechanics model. The total strain ε_T was then composed of elastic strain ε_{el}, diffusion-induced strain ε_{diff}, and thermal strain ε_{th}.

$$\varepsilon_T = \varepsilon_{el} + \varepsilon_{diff} + \varepsilon_{th} \tag{13}$$

The electrode was assumed to be an isotropic, linear elastic solid. Elastic strain was computed by the following linear elastic constitutive equation:[56]

$$\varepsilon_{ij}^{el} = \frac{1}{E}\left[(1 + \upsilon)\tau_{ij} - \upsilon\tau_{kk}\delta_{ij}\right] \tag{14}$$

where E is Young's modulus, υ is Poisson's ratio, τ is the stress tensor, and δ is the Kronecker delta. To consider the phase transformation between LiFePO$_4$ and FePO$_4$, concentration-dependent material properties were incorporated. The material property matrix $[K]$ was defined as

$$K(x) = x[K]^{LiFePO_4} + (1 - x)[K]^{FePO_4} \tag{15}$$

where x represents the fraction of lithium-rich phase ($0 \leq x \leq 1$). The detailed material properties for the mechanical model were described in our previous work.[42]

In this study, we used a hygroscopic swelling analysis in COMSOL to investigate stress evolutions caused by lithium-ion diffusion. Specifically, hygroscopic swelling was analogous to the volume expansion and/or contraction due to lithiation in the electrode and is expressed below:

$$\varepsilon_{ij}^{dis} = \beta\Delta C\delta_{ij} \tag{16}$$

where β is the coefficient of hygroscopic swelling (i.e., volume expansion) and ΔC is the change in lithium-ion concentration. In this study, coefficient of hygroscopic swelling was assumed to be constant, β = 6%, over discharging and charging processes.

Based on the experimental work by Panchal et al.,[28] a LiFePO$_4$ pouch cell had shown dramatic temperature increase
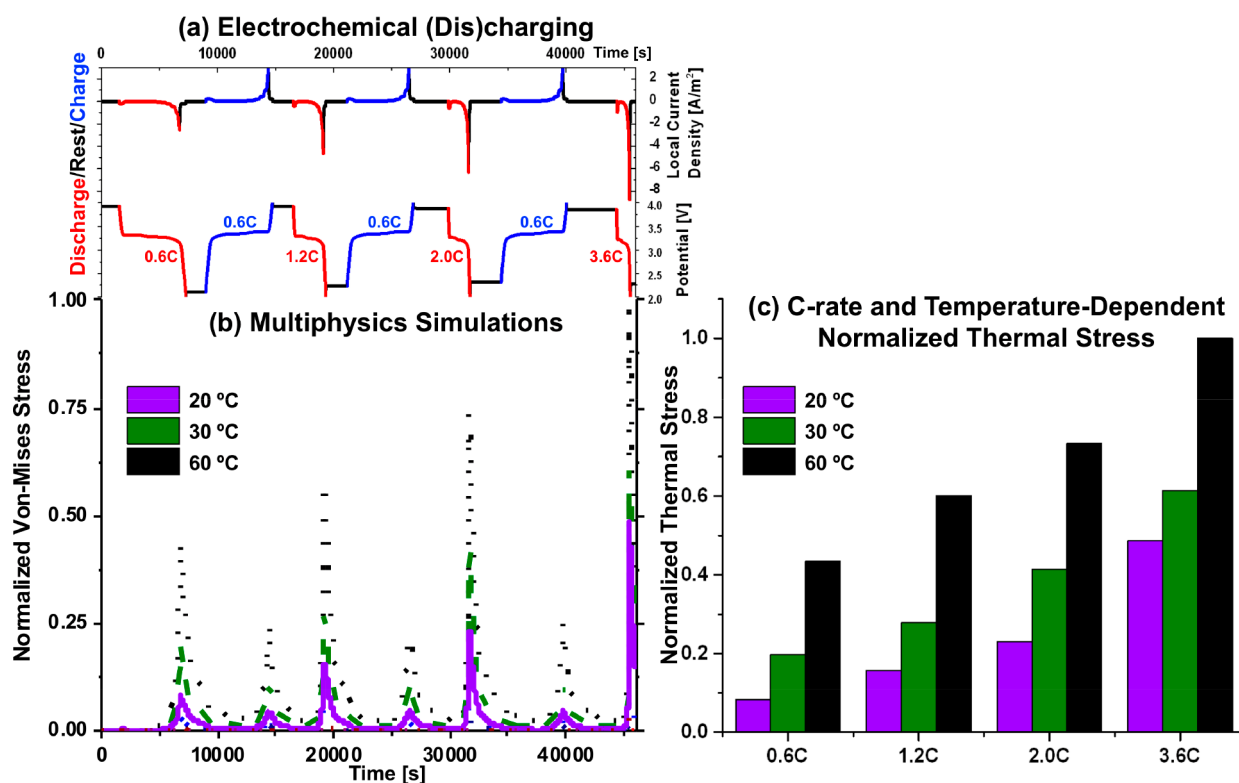
Figure 5. (a) Local current density and potentials vs time for multiphysic computational simulations. (b) Normalized thermal stress vs time demonstrating effects of ambient temperatures and C-rates on thermal stresses. (c) Normalized thermal stress values at different C-rates at different ambient temperatures.

at high C-rate (dis)charging. Thus, thermal strain was included in this study and is described by the following equation:

$$\varepsilon_{ij}^{\text{th}} = \alpha_{c,l}\Delta T\delta_{ij} \qquad (17)$$

where α is the thermal expansion coefficient of cathode or electrolyte and ΔT is the temperature change. Thermal expansion of electrolyte was also considered, and the coefficient of thermal expansion is shown in Table 2.

3. RESULTS AND DISCUSSION

3.1. Electrochemical Testing and Temperature Change. During electrochemical testing, the local current density reached −2.54, −4.61, −6.29, and −8.88 A/m^2 at the 0.6, 1.2, 2.0, and 3.6 discharging rates, respectively, while the local current density reached 2.93−2.97 A/m^2 at 0.6 charging rate (Figure 4a). The corresponding potential variations are presented in Figure 4a.

The total (dis)charging time was also recorded. It was observed that the total discharging time was ∼6000 s at 0.6C, ∼3000 s at 1.2C, ∼1800 s at 2C, and ∼1000 s at 3.6C. Figure 1c shows temperature variations during discharging at different C-rates (0.6C, 1.2C, 2.0C, and 3.6C). Even though Joule heating was the only heat source considered, the results from the multiphysic simulations matched well with the FBG measurements. It confirms Joule heating as the main heat source in lithium-ion batteries during cycling, and other heat sources (i.e., entropy heat, chemical side reactions, heat of mixing) are negligible. From both experimental and simulation results, it was observed that higher C-rate showed higher temperature change, suggesting that higher Joule heating was generated at higher C-rate, and this phenomenon was also

observed in LiCoO$_2$ battery chemistry.[40] The temperature changes, ΔT, measured with the FBG sensors were 2.09, 5.22, 8.75, and 13.75 °C at 0.6C, 1.2C, 2C, and 3.6C, respectively. At 1.2C and 2C, the root-mean-square error (RMSE) of temperature change ΔT between the simulated and measured data was less than 0.1%, and the RMSE at 0.6C and 3.6C was 3.87% and 3.49%, respectively. From these results, we concluded that the predicted temperature changes from the simulations demonstrated good agreement with experimental data from FBG measurements.

Based on the total discharging time at different C-rates, the state of charge (SoC) is calculated by normalizing the discharging time. For example, a total of ∼6000 s of discharging at 0.6C indicates that 25% of discharging (i.e., SoC = 0.25) occurs at 1500 s and 90% of discharging (i.e., SoC = 0.9) occurs at 5400 s; a total of ∼1000 s for discharging at 3.6C indicates that 25% of discharging (i.e., SoC = 0.25) occurs at 250 s and 90% of discharging (i.e., SoC = 0.9) occurs at 900 s, etc. The temperature gradients at the beginning (i.e., SoC < 0.23) and the end (i.e., SoC > 0.9) of the discharging process were higher than that of the plateau region of discharging (i.e., 0.23 < SoC < 0.9) for all measured and simulation cells. A similar phenomenon was observed in the previous study by Saw et al.[27] and Panchal et al.,[28] where they showed the gradients of total heat were relatively high at the beginning and at the end of the discharging process. It is suggested that the activation polarization due to the limited reaction rate at the beginning of discharging and the concentration polarization from limited mass transport at the end of discharging have both caused higher heat generation than that from the ohmic polarization.

3.2. Concentration Distribution. The results of computational electrochemical simulations were verified by comparing
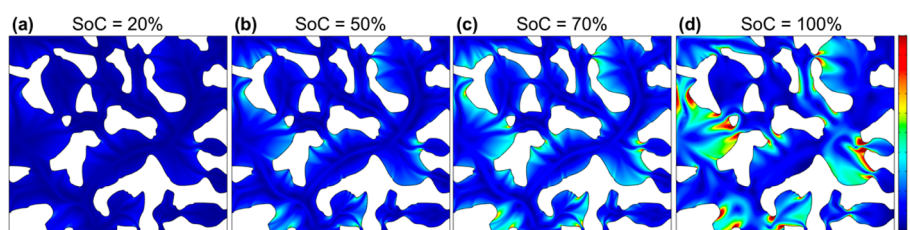
Figure 6. Diffusion-induced stress at different SoCs. Higher stresses were observed at the connecting areas between particles at the end of the discharging process, suggesting that the higher stresses might result from higher concentration variations in the connecting area. Scale bar: normalized concentration was used.

electrochemical testing on 14 430 lithium-ion cells at four different discharging rates (0.6C, 1.2C, 2.0C, and 3.6C) and at a charging rate of 0.6C between 2.0 and 4.0 V. In the computational simulations, electrochemical (dis)charging sequences followed experimental electrochemical testing. The electrode was discharged at 0.6C (2000−8000 s), 1.2C (17 000−20 000 s), 2.0C (30 400−32 200 s), and 3.6C (45 000−46 000 s) with charging at 0.6C in between (9450− 15 200 s, 21 600−27 300 s, and 34 900−40 500 s) (Figure 4a). Initial concentration in the electrode was assumed to be 5000 mol/m^3. Based on eqs 2−10, concentration distributions in the electrode at different C-rates could be determined (Figure 4b). Concentration profiles during (dis)charging at four different locations denoted as P1, P2, P3, and P4 were compared, where P1 and P2 indicate outer layer and P3 and P4 indicate the connecting area between each active particle and inside of an active particle, respectively (Figure 4c). It was observed that lithium-ion concentration distribution was location dependent where lithium ions diffuse from the outer layer to the inside of the particle. That is, at any time and given C-rate, P1 and P2 located on the outer layer of the particle revealed higher concentrations than those of P3 and P4, which are located inside of the particles (Figure 4b). Particularly, the concentration at the surface of the particle indicated in black and blue lines (P1 and P2) showed nearly the same concentration due to the same local current density applied. Moreover, the gap between P3 and the other points (i.e., P1, P2, and P4) gradually increases at the end of discharging as C-rate increases. This suggested that the concentration distribution become non-homogeneous in the cathode under higher C-rate. Figure 4c demonstrates concentration evolutions for the reconstructed porous microstructures of LiFePO$_4$ at different SoCs. Compared to larger particles, smaller particles showed higher concentrations, indicating more dramatic concentration variations were observed in smaller particles. Comparing to our previous study by adopting core−shell models,[42] we have used the same local current density as the boundary condition on the particle surface; the concentration distributions in this study were different from the ones obtained from mostly adopted core−shell models. It is suggested that reconstructed porous microstructures of LiFePO$_4$ could possibly provide more details on concentration evolutions during (dis)charging at different C-rates.

3.3. Mechanical Stresses. *3.3.1. Thermal Stress.* With the prescribed electrochemical (dis)charging sequences, discharged at 0.6C, 1.2C, 2.0C, and 3.6C and with 0.6C charging in between, thermal stress variations at three different ambient temperatures under different C-rates were obtained (Figure 5b). The results showed that by increasing C-rate from 0.6C to 3.6C (i.e., discharging 6 times faster), it resulted in 5.92, 3.11, and 2.30 times higher thermal stresses at 20, 30, and 60 °C,

respectively. It suggested that the effects of C-rate were more critical at room temperature (i.e., 25 °C) than that at higher temperature (i.e., 60 °C). In spite of a sharp decrease in potential at the beginning of discharging, thermal stresses and temperature increased more dramatically at the end of discharging, compared to that at the beginning of discharging. Our results confirmed that effects of increasing temperature results in larger thermal stresses during (dis)charging. More-over, it is observed that thermal stress during the discharging process is higher than that during the charging process under the same C-rate. Figure 5b also demonstrates that increases in thermal stress due to higher temperature played a lesser role at higher C-rates. For example, if nondimensionalization was used for thermal stresses by setting the thermal stress value to 1 at 60 °C at 3.6C discharging rate, thermal stress is 2.06 times higher than that at 20 °C (1/0.48638 = 2.06) and 1.63 times higher than that at 30 °C (1/0.61421 = 1.63), whereas thermal stress at 60 °C is 5.29 times higher than that at 20 °C (0.43505/ 0.08219 = 5.29) and 2.20 times higher than that at 30 °C (0.43505/0.19771 = 2.2) at 0.6C discharging rate, as shown in Figure 5c. This can be explained by the fact that heat generation inside lithium-ion battery was more critical compared to heat convention to the environment, whereas relatively lower heat generation in lower C-rate inside battery resulted in critical heat convention. Because higher external temperature was highly related to heat convention, therefore effects of higher external temperature played a much higher role at lower C-rate.

3.3.2. Diffusion-Induced Stress. Since the magnitudes of thermal stresses in electrodes were much smaller than those of diffusion-induced stresses, to demonstrate the evolution of overall stresses across the entire range of SoC, diffusion-induced stresses from 20% to 100% SoC at 3.6C were presented (Figure 6). Higher stresses were observed at the connecting areas between particles, suggesting that the higher stresses might result from higher concentration variations in the connecting area. Compared to other previous results where only homogeneous spherical particles were considered,[10,38,42,57] the current study showed that reconstructed microstructures of electrode particles were very important for stress analysis, and it is hypothesized that it is highly related to crack initiations.[58]

The rate capability of 14 430 lithium-ion cells performed via a 273A potentiostat/galvanostat at different discharging rates (1.2C, 2.0C, and 3.6C) is shown in Figure 7a, and the capacity lost was recorded. The results showed that 14 430 lithium-ion cells tested at 3.6C have 30% capacity loss compared to cells tested at 1.2C; a corresponding 150% increase in stress was observed from the multiphysic simulations, where both thermal and diffusion-induced stresses were included (Figure 7b). Note that normalized stresses and normalized capacities were used in Figure 7 for clear comparisons. At all C-rates, stresses increase
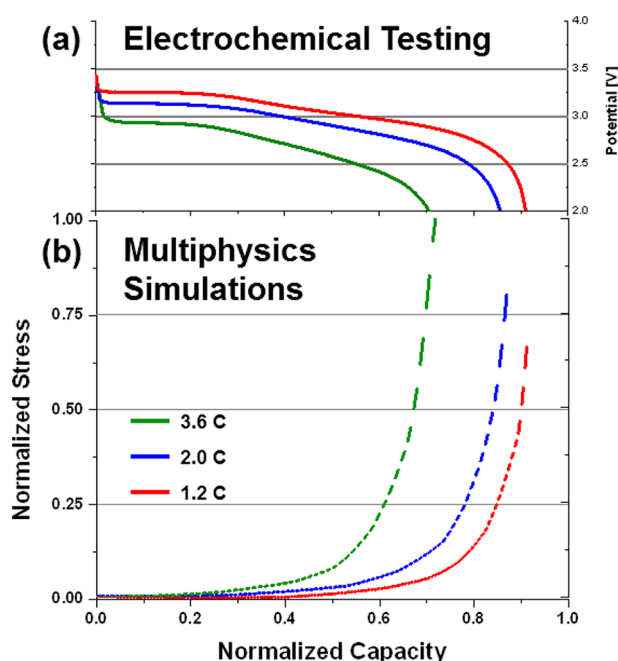
Figure 7. (a) Experimental capacity losses in 1.2C, 2.0C, and 3.6C was observed. Almost 30% capacity loss was observed at 3.6C compared to cells tested at 1.2C. (b) Simulation results revealed 150% increased stresses at 3.6C compared to cells at 1.2C. For clearer comparisons, normalized stresses (combination of thermal and diffusion-induced stresses) and normalized capacity were used. It is suggested that larger capacity loss was mainly caused by higher stresses at higher C-rates.

significantly at the end of the discharging process and may be related to dramatic drops in potential at the end of discharging. It was concluded that higher capacity loss at the higher C-rate (e.g., 30% loss at 3.6C) was mainly caused by higher stresses at higher C-rate (e.g., 150% increase in stresses at 3.6C). The capacity fades measured from the potentiostat were 10%, 13%, and 27% at 1.2C, 2.0C, and 3.6C, respectively (Figure 7a). The simulation results show that the capacity fade was 6%, 9%, 14%, and 30% at 0.6C, 1.2C, 2.0C, and 3.6C, respectively (Figure 7b).

3.3.3. Limitations of the Study. In these efforts to experimentally measure *in operando* temperature variation and computationally simulate thermal and mechanical effects during lithium-ion battery discharging with reconstructed microstructure, several limitations existed in the current study. Based on the results from Kupper and Bessler,[59] the temperature distribution is considered uniform in the electrode since temperature gradients occur on a larger scale (e.g., mm and/or cm) compared to the particle size (e.g., nm and/or μm). Thus, only temperature "variation" vs time was reported (Figure 1) and used to predict thermal stresses (Figure 5). Furthermore, carbon black and PVDF binder were not included in the reconstructed microstructure in this study, and effects from these components will be further identified in future work. Though the coupled electrochemistry of electrolyte and electrode was studied in this work, to reduce computational time the solid electrolyte interface was not explicitly considered in the model.

4. CONCLUSIONS

In this paper, computational models incorporating coupled electrochemical–mechanical–thermal factors were used to

investigate the relationships between mechanical stresses and capacity loss in lithium-ion batteries. Further, reconstructed microstructures of LiFePO₄ were used to enhance the accuracy of the predicted stresses in batteries. Electrochemical–thermal models were verified by experimental measurements, including temperature variations measured via FBG sensors and capacity loss measured via a potentiostat/galvanostat. The experimentally verified multiphysics models had predicted thermal stresses, potential variations, concentration evolutions, and mechanical stresses during (dis)charging at different external temperatures and C-rates. Furthermore, effects of ambient temperatures and C-rates on thermal stress have been investigated, and it was observed that increasing temperature and C-rate results in larger thermal stresses during (dis)-charging. However, at higher C-rates, increases in thermal stresses due to higher temperature played a lesser role. Moreover, concentration evolution in the reconstructed cathode has been presented. As expected, higher concentration and dramatic concentration changes were exhibited at the surface of particles as compared to those at the center of the particles. Higher concentration variation also appeared at connecting areas between particles. Moreover, it is also confirmed that the concentration distribution becomes non-homogenous at higher C-rates. By comparing diffusion-induced stress with thermal stress, it was concluded that the effects of diffusion-induced stress dominated in the cathode. With a simple 2D model by integrating some key factors occurring in battery (dis)charging while neglecting other details (i.e., polarizations, carbon black, etc.), a relationship between mechanical stresses and capacity fade was also observed before particle crack initiation. On the basis of the methodology and results presented in this paper, we can further study particle crack prediction and battery degradation in a 3D system.

■ AUTHOR INFORMATION

Corresponding Author
*(H.-Y.S.H.) Tel 919.513.0798; Fax 919.515.7968; e-mail hshuang@ncsu.edu.

ORCID ⓘ
Hsiao-Ying Shadow Huang: 0000-0002-5647-7049

Notes
The authors declare no competing financial interest.

■ REFERENCES

(1) Kumar, A.; Thomas, R.; Karan, N. K.; Saavedra-Arias, J. J.; Singh, M. K.; Majumder, S. B.; Tomar, M. S.; Katiyar, R. S. Structural and Electrochemical Characterization of Pure LiFePO₄ and Nanocomposite C-LiFePO₄ Cathodes for Lithium Ion Rechargeable Batteries. *J. Nanotechnol.* **2009**, *2009*, 1–10.
(2) Cho, Y.-D.; Fey, G. T.-K.; Kao, H.-M. The Effect of Carbon Coating Thickness on the Capacity of LiFePO₄/C Composite Cathodes. *J. Power Sources* **2009**, *189*, 256–262.
(3) Guerfi, A.; Ravet, N.; Charest, P.; Dontigny, M.; Petitclerc, M.; Gauthier, M.; Zaghib, K. Temperature Effects on LiFePO₄ Cathode Performance. *ECS Trans.* **2006**, *3*, 3–17.
(4) Dupré, N.; Cuisinier, M.; Martin, J. F.; Guyomard, D. Interphase Evolution at Two Promising Electrode Materials for Li-Ion Batteries: LiFePO₄ and LiNi₁/₂Mn₁/₂O₂. *ChemPhysChem* **2014**, *15*, 1922–1938.
(5) Dupré, N.; Martin, J.-F.; Degryse, J.; Fernandez, V.; Soudan, P.; Guyomard, D. Aging of the LiFePO₄ Positive Electrode Interface in Electrolyte. *J. Power Sources* **2010**, *195*, 7415–7425.
(6) Aurbach, D.; Markovsky, B.; Salitra, G.; Markevich, E.; Talyossef, Y.; Koltypin, M.; Nazar, L.; Ellis, B.; Kovacheva, D. In Review on Electrode–electrolyte Solution Interactions, Related to Cathode

Materials for Li-Ion Batteries, Proceedings of the International Battery Association & Hawaii Battery Conference 2006, Waikoloa, HI, Jan 9–12, 2006.

(7) Meethong, N.; Huang, H. Y. S.; Speakman, S. A.; Carter, W. C.; Chiang, Y. M. Strain Accommodation during Phase Transformations in Olivine-Based Cathodes as a Materials Selection Criterion for High-Power Rechargeable Batteries. *Adv. Funct. Mater.* **2007**, *17*, 1115–1123.

(8) Meethong, N.; Huang, H.-Y. S.; Carter, W. C.; Chiang, Y.-M. Size-Dependent Lithium Miscibility Gap in Nanoscale $Li_{1-x}FePO_4$. *Electrochem. Solid-State Lett.* **2007**, *10*, A134–A138.

(9) Li, J.; Zhang, Q.; Xiao, X.; Cheng, Y. T.; Liang, C.; Dudney, N. J. Unravelling the Impact of Reaction Paths on Mechanical Degradation of Intercalation Cathodes for Lithium-Ion Batteries. *J. Am. Chem. Soc.* **2015**, *137*, 13732–13735.

(10) Park, J.; Lu, W.; Sastry, A. M. Numerical Simulation of Stress Evolution in Lithium Manganese Dioxide Particles due to Coupled Phase Transition and Intercalation. *J. Electrochem. Soc.* **2011**, *158*, A201.

(11) Sheem, K. Y.; Sung, M.; Lee, Y. H. Electrostatic Hetero-coagulation of Carbon Nanotubes and $LiCoO_2$ Particles for a High-Performance Li-Ion Cell. *Electrochim. Acta* **2010**, *55*, 5808–5812.

(12) Qi, Y.; Harris, S. J. In Situ Observation of Strains during Lithiation of a Graphite Electrode. *J. Electrochem. Soc.* **2010**, *157*, A741–A747.

(13) Chan, C. K.; Patel, R. N.; O'Connell, M. J.; Korgel, B. A.; Cui, Y. Solution-Grown Silicon Nanowires for Lithium-Ion Battery Anodes. *ACS Nano* **2010**, *4*, 1443–1450.

(14) Li, Y.; El Gabaly, F.; Ferguson, T. R.; Smith, R. B.; Bartelt, N. C.; Sugar, J. D.; Fenton, K. R.; Cogswell, D. A.; Kilcoyne, A. L. D.; Tyliszczak, T.; et al. Current-Induced Transition from Particle-by-Particle to Concurrent Intercalation in Phase-Separating Battery Electrodes. *Nat. Mater.* **2014**, *13*, 1149–1156.

(15) Wang, D.; Wu, X.; Wang, Z.; Chen, L. Cracking Causing Cyclic Instability of $LiFePO_4$ Cathode Material. *J. Power Sources* **2005**, *140*, 125–128.

(16) Nyman, A.; Behm, M.; Lindbergh, G. Electrochemical Characterisation and Modelling of the Mass Transport Phenomena in $LiPF_6$-EC-EMC Electrolyte. *Electrochim. Acta* **2008**, *53*, 6356–6365.

(17) Nyman, A.; Behm, M.; Lindbergh, G. A Theoretical and Experimental Study of the Mass Transport in Gel Electrolytes II. Experimental Characterization of $LiPF_6$-EC-PC-P(VdF-HFP). *J. Electrochem. Soc.* **2011**, *158*, A636.

(18) Prada, E.; Di Domenico, D.; Creff, Y.; Bernard, J.; Sauvant-Moynot, V.; Huet, F. A Simplified Electrochemical and Thermal Aging Model of $LiFePO_4$-Graphite Li-ion Batteries: Power and Capacity Fade Simulations. *J. Electrochem. Soc.* **2013**, *160*, A616–A628.

(19) Edström, K.; Gustafsson, T.; Thomas, J. O. The Cathode–electrolyte Interface in the Li-Ion Battery. *Electrochim. Acta* **2004**, *50*, 397–403.

(20) JU, H.; WU, J.; XU, Y. Revisiting the Electrochemical Impedance Behaviour of the $LiFePO_4$/C Cathode. *J. Chem. Sci.* **2013**, *125*, 687–693.

(21) Aurbach, D.; Talyosef, Y.; Markovsky, B.; Markevich, E.; Zinigrad, E.; Asraf, L.; Gnanaraj, J. S.; Kim, H. J. Design of Electrolyte Solutions for Li and Li-Ion Batteries: A Review. *Electrochim. Acta* **2004**, *50*, 247–254.

(22) Ahmed, S.; Bloom, I.; Jansen, A. N.; Tanim, T.; Dufek, E. J.; Pesaran, A.; Burnham, A.; Carlson, R. B.; Dias, F.; Hardy, K.; et al. Enabling Fast Charging – A Battery Technology Gap Assessment. *J. Power Sources* **2017**, *367*, 250–262.

(23) Keyser, M.; Ahmad, P.; Li, Q.; Santhanagopalan, S.; Smith, K.; Wood, E.; Shabbir, A.; Bloom, I.; Dufek, E.; Shirk, M.; et al. Enabling Fast Charging - Battery Thermal Considerations. *J. Power Sources* **2017**, *367*, 228–236.

(24) Liu, B.; Zhao, H.; Yu, H.; Li, J.; Xu, J. Electrochimica Acta Multiphysics Computational Framework for Cylindrical Lithium-Ion Batteries under Mechanical Abusive Loading. *Electrochim. Acta* **2017**, *256*, 172–184.

(25) Xu, J.; Liu, B.; Wang, X.; Hu, D. Computational Model of 18650 Lithium-Ion Battery with Coupled Strain Rate and SOC Dependencies. *Appl. Energy* **2016**, *172*, 180–189.

(26) Liu, B.; Yin, S.; Xu, J. Integrated Computation Model of Lithium-Ion Battery Subject to Nail Penetration. *Appl. Energy* **2016**, *183*, 278–289.

(27) Saw, L. H.; Ye, Y.; Tay, A. A. O. Electrochemical-Thermal Analysis of 18650 Lithium Iron Phosphate Cell. *Energy Convers. Manage.* **2013**, *75*, 162–174.

(28) Panchal, S.; Dincer, I.; Agelin-Chaab, M.; Fraser, R.; Fowler, M. Experimental and Theoretical Investigations of Heat Generation Rates for a Water Cooled LiFePO4 Battery. *Int. J. Heat Mass Transfer* **2016**, *101*, 1093–1102.

(29) Lee, S. J.; Lee, C. Y.; Chung, M. Y.; Chen, Y. H.; Han, K. C.; Liu, C. K.; Yu, W. C.; Chang, Y. M. Lithium-Ion Battery Module Temperature Monitoring by Using Planer Home-Made Micro Thermocouples. *Int. J. Electrochem. Sci.* **2013**, *8*, 4131–4141.

(30) Forgez, C.; Vinh Do, D.; Friedrich, G.; Morcrette, M.; Delacourt, C. Thermal Modeling of a Cylindrical LiFePO4/graphite Lithium-Ion Battery. *J. Power Sources* **2010**, *195*, 2961–2968.

(31) Mathewson, S. Experimental Measurements of $LiFePO_4$ Battery Thermal Characteristics, M.S. Thesis, University of Waterloo, Waterloo, ON, 2014.

(32) Lee, C. Y.; Lee, S. J.; Tang, M. S.; Chen, P. C. In Situ Monitoring of Temperature inside Lithium-Ion Batteries by Flexible Micro Temperature Sensors. *Sensors* **2011**, *11*, 9942–9950.

(33) Fiber Bragg Grating Sensors. *Encyclopedia of Structural Health Monitoring [Online]*; John Wiley & Sons: Posted Sept 15, 2009; http://onlinelibrary.wiley.com/doi/10.1002/9780470061626.shm024/full.

(34) Meyer, J.; Nedjalkov, A.; Doering, A.; Angelmahr, M.; Schade, W. In Fiber Optical Sensors for Enhanced Battery Safety, Proceedings of Fiber Optic Sensors and Applications XII, Baltimore, MD, Apr 20–24, 2015.

(35) Novais, S.; Nascimento, M.; Grande, L.; Domingues, M. F.; Antunes, P.; Alberto, N.; Leitão, C.; Oliveira, R.; Koch, S.; Kim, G. T.; et al. Internal and External Temperature Monitoring of a Li-Ion Battery with Fiber Bragg Grating Sensors. *Sensors* **2016**, *16*, 1394.

(36) Zhang, X.; Sastry, A. M.; Shyy, W. Intercalation-Induced Stress and Heat Generation within Single Lithium-Ion Battery Cathode Particles. *J. Electrochem. Soc.* **2008**, *155*, A542–A552.

(37) Wu, W.; Xiao, X.; Huang, X.; Yan, S. A Multiphysics Model for the in Situ Stress Analysis of the Separator in a Lithium-Ion Battery Cell. *Comput. Mater. Sci.* **2014**, *83*, 127–136.

(38) Xiao, X.; Wu, W.; Huang, X. A Multi-Scale Approach for the Stress Analysis of Polymeric Separators in a Lithium-Ion Battery. *J. Power Sources* **2010**, *195*, 7649–7660.

(39) Wu, W.; Xiao, X.; Shi, D. In Heat Transfer and Thermal Stress in a Lithium-Ion Battery, Proceedings of the ASME 2010 International Mechanical Engineering Congress & Exposition, Vancouber, BC, Nov 12–18, 2010.

(40) Yan, B.; Lim, C.; Yin, L.; Zhu, L. Simulation of Heat Generation in a Reconstructed $LiCoO_2$ Cathode during Galvanostatic Discharge. *Electrochim. Acta* **2013**, *100*, 171–179.

(41) Doyle, M.; Newman, J. The Use of Mathematical Modeling in the Design of Lithium/polymer Battery Systems. *Electrochim. Acta* **1995**, *40*, 2191–2196.

(42) Kim, S.; Huang, H.-Y. S. Mechanical Stresses at the Cathode–electrolyte Interface in Lithium-Ion Batteries. *J. Mater. Res.* **2016**, *31*, 3506–3512.

(43) Mukhopadhyay, A.; Sheldon, B. W. Deformation and Stress in Electrode Materials for Li-Ion Batteries. *Prog. Mater. Sci.* **2014**, *63*, 58–116.

(44) Kashkooli, A. G.; Farhad, S.; Lee, D. U.; Feng, K.; Litster, S.; Babu, S. K.; Zhu, L.; Chen, Z. Multiscale Modeling of Lithium-Ion Battery Electrodes Based on Nano-Scale X-Ray Computed Tomography. *J. Power Sources* **2016**, *307*, 496–509.

(45) Wu, L.; Xiao, X.; Wen, Y.; Zhang, J. Three-Dimensional Finite Element Study on Stress Generation in Synchrotron X-Ray

Tomography Reconstructed Nickel-Manganese-Cobalt Based Half Cell. *J. Power Sources* **2016**, *336*, 8−18.

(46) Wiedemann, A. H.; Goldin, G. M.; Barnett, S. A.; Zhu, H.; Kee, R. J. Effects of Three-Dimensional Cathode Microstructure on the Performance of Lithium-Ion Battery Cathodes. *Electrochim. Acta* **2013**, *88*, 580−588.

(47) Roberts, S. A.; Brunini, V. E.; Long, K. N.; Grillet, a. M. A Framework for Three-Dimensional Mesoscale Modeling of Anisotropic Swelling and Mechanical Deformation in Lithium-Ion Electrodes. *J. Electrochem. Soc.* **2014**, *161*, F3052−F3059.

(48) Ender, M.; Joos, J.; Carraro, T.; Ivers-Tiffee, E. Quantitative Characterization of LiFePO$_4$ Cathodes Reconstructed by FIB/SEM Tomography. *J. Electrochem. Soc.* **2012**, *159*, A972−A980.

(49) Liu, Z.; Chen-Wiegart, Y. K.; Wang, J.; Barnett, S. A.; Faber, K. T. Three-Phase 3D Reconstruction of a LiCoO$_2$ Cathode via FIB-SEM Tomography. *Microsc. Microanal.* **2016**, *22*, 140−148.

(50) Hutzenlaub, T.; Thiele, S.; Paust, N.; Spotnitz, R.; Zengerle, R.; Walchshofer, C. Three-Dimensional Electrochemical Li-Ion Battery Modelling Featuring a Focused Ion-Beam/scanning Electron Microscopy Based Three-Phase Reconstruction of a LiCoO$_2$ Cathode. *Electrochim. Acta* **2014**, *115*, 131−139.

(51) Malavé, V.; Berger, J. R.; Zhu, H.; Kee, R. J. A Computational Model of the Mechanical Behavior within Reconstructed LixCoO$_2$ Li-Ion Battery Cathode Particles. *Electrochim. Acta* **2014**, *130*, 707−717.

(52) Song, B.; Sui, T.; Ying, S.; Li, L.; Lu, L.; Korsunsky, A. M. Nano-Structural Changes in Li-Ion Battery Cathodes during Cycling Revealed by FIB-SEM Serial Sectioning Tomography. *J. Mater. Chem. A* **2015**, *3*, 18171−18179.

(53) COMSOL Multiphysics, version 5.2a; software for mutlphysics simulation; COMSOL, 2016.

(54) Shadow Huang, H.-Y.; Wang, Y.-X. Dislocation Based Stress Developments in Lithium-Ion Batteries. *J. Electrochem. Soc.* **2012**, *159*, A815−A821.

(55) Shi, D. Stress Analysis Of the Separator in a Lithium-Ion Battery, M.S. Thesis, Michigan State University, East Lansing, MI, 2010.

(56) Slaughter, W. S. *Constitutive Eqautions. The Linearized Theory of Elasticity*; Birkhäuser: Boston, 2002; pp 193−220.

(57) Song, J.; Kim, J.; Kang, T.; Kim, D. Design of a Porous Cathode for Ultrahigh Performance of a Li-Ion Battery: An Overlooked Pore Distribution. *Sci. Rep.* **2017**, *7*, 42521.

(58) Chiuhuang, C.; Huang, H. S. Critical Lithiation for C-Rate Dependent Mechanical Stresses in LiFePO$_4$. *J. Solid State Electrochem.* **2015**, *19*, 2245−2253.

(59) Kupper, C.; Bessler, W. G. Multi-Scale Thermo-Electrochemical Modeling of Performance and Aging of a LiFePO4/Graphite Lithium-Ion Cell. *J. Electrochem. Soc.* **2017**, *164*, A304−A320.

(60) Li, X.; Choe, S. Y.; Joe, W. T. A Reduced Order Electrochemical and Thermal Model for a Pouch Type Lithium Ion Polymer Battery with LiNi$_x$Mn$_y$Co$_{1-x-y}$O$_2$/LiFePO$_4$ Blended Cathode. *J. Power Sources* **2015**, *294*, 545−555.

(61) Tanim, T. R.; Rahn, C. D.; Wang, C. Y. State of Charge Estimation of a Lithium Ion Cell Based on a Temperature Dependent and Electrolyte Enhanced Single Particle Model. *Energy* **2015**, *80*, 731−739.

(62) Park, M.; Zhang, X.; Chung, M.; Less, G. B.; Sastry, A. M. A Review of Conduction Phenomena in Li-Ion Batteries. *J. Power Sources* **2010**, *195*, 7904−7929.

(63) Taleghani, S. T.; Marcos, B.; Zaghib, K.; Lantagne, G. A Study on the Effect of Porosity and Particles Size Distribution on Li-Ion Battery Performance. *J. Electrochem. Soc.* **2017**, *164*, E3179−E3189.

(64) Bahiraei, F.; Ghalkhani, M.; Fartaj, A.; Nazri, G.-A. A Pseudo 3D Electrochemical-Thermal Modeling and Analysis of a Lithium-Ion Battery for Electric Vehicle Thermal Management Applications. *Appl. Therm. Eng.* **2017**, *125*, 904−918.

(65) Adams, S.; P. Rao, R. Design of (Thio) Phosphates for High Performance Lithium Ion Batteries. *Ceram. Mater. Energy Appl.* **2011**, *32*, 161−176.